Materials and Design 180 (2019) 107962

Contents lists available at ScienceDirect

Materials and Design

journal homepage: www.elsevier.com/locate/matdes

Simulation of failure processes of as-cast Ti-5Al-5Nb-1Mo-1V-1Fe titanium alloy subjected to quasi-static uniaxial tensile testing

Haichao Gong, Qunbo Fan *, Yu Zhou, Duoduo Wang, Pengru Li, Tiejian Su, Hongmei Zhang

School of Materials Science and Engineering, Beijing Institute of Technology, Beijing 100081, China
National Key Laboratory of Science and Technology on Materials Under Shock and Impact, Beijing 100081, China

HIGHLIGHTS

- The three-dimensional porous microstructure of a cast titanium alloy was obtained through micro-computed tomography.
- The process of damage and fracture under uniaxial tension was simulated by finite element techniques.
- Multiaxial principal stress concentration dominated steady propagation of cracks.
- Shear stress concentration dominated unstable propagation of cracks.

GRAPHICAL ABSTRACT

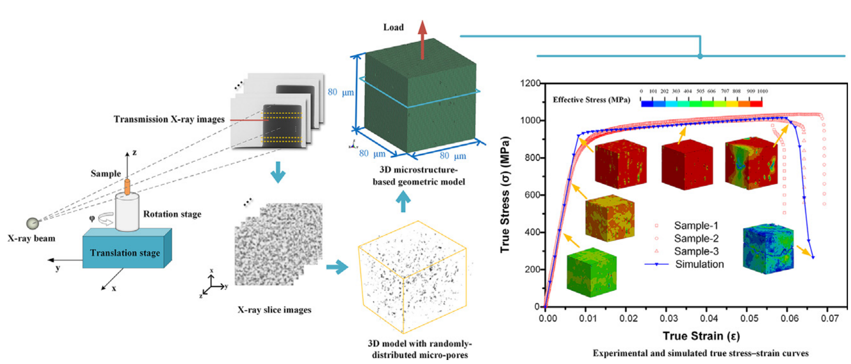

ARTICLE INFO

Article history:
Received 19 April 2019
Received in revised form 3 June 2019
Accepted 20 June 2019
Available online 21 June 2019

Keywords:
As-cast titanium alloy
Microstructures
Triaxiality
Failure mode

ABSTRACT

A three-dimensional (3D) microscopic structural finite element model reflecting the realistic pore distribution of as-cast Ti-5Al-5Nb-1Mo-1V-1Fe titanium alloy was built through micro-computed tomography (micro-CT). The model was then introduced into ANSYS LS-DYNA software to investigate the 3D spatial evolution process of damage and failure under quasi-static uniaxial tension. To validate the simulation results, we tested the uniaxial tensile responses of Ti-5Al-5Nb-1Mo-1V-1Fe and quantitatively characterized the tensile fracture morphology with a 3D profilometer. To reveal the underlying mechanism of damage and failure, we took the triaxiality of R_σ into consideration. Local principal stress concentration was found to exist around two micro-pores at the initial stage, thus inducing two crack sources; as the load increased, more crack sources were generated and steadily propagated through void growth and coalescence under the influence of multiaxial principal stress concentration, thus leading to the local tensile failure of the model. When cracks reached a critical size, the shear stress concentration became the dominant factor affecting failure, thus inducing severe effective plastic strain between cracks. The cracks rapidly connected through plastic slip and cleavage, thereby resulting in the final shear failure of the model. The simulation results were in good agreement with the observed experimental results.

1. Introduction

The development and application of high performance titanium alloy castings in structural components in harsh environments such as aerospace and marine environments is highly important [1]. First,

* Corresponding author at: School of Materials Science and Engineering, Beijing Institute of Technology, Beijing 100081, China.
E-mail address: fanqunbo@bit.edu.cn (Q. Fan).

https://doi.org/10.1016/j.matdes.2019.107962

titanium alloys, compared with steel materials, have superior properties such as lower density, higher specific strength and corrosion resistance, which can improve structural efficiency; in addition, it has higher strength and higher temperature resistance than aluminum alloys [2–4]. Second, near net shaping of titanium alloy castings reduces processing steps and fasteners, thereby saving material, time and cost as well as weight [4–6]. However, the castability of titanium alloys is poor, mainly because of their poor fluidity and high sensitivity to elements such as nitrogen, oxygen and hydrogen in the molten state; consequently, gas holes and shrinkage pores are easily generated [4,7–9]. The existence of pores leads to imperfections in the materials as well as concentration of local stress, thus negatively influencing the performance and reliability of the materials [10], and possibly resulting in premature failure of titanium alloy structural components [7]. To provide a valuable data reference for safe use of titanium alloy castings, it is crucial to study pore evolution and the mechanic fields around them during the loading procedure, as well as their effects on the failure of as-cast titanium alloys [11].

Optical microscopy (OM) and scanning electron microscopy (SEM) are commonly used to characterize the distribution and morphology of pores in materials [12–16]. Ye et al. [14] have studied the distribution, quantity and morphology of in-situ graded microporous structures of several titanium alloys by SEM, and have carried out tension and compression tests to study the effects of graded micro-pores on the mechanical properties. Chen et al. [15] have systematically studied the morphology of pores and the element distribution around the pores of the selective-laser-melted Ti-37Nb-6Sn alloy by using SEM and electron probe microanalysis, and have analyzed defect formation and its influence on mechanical behavior. However, the microstructural characteristics of the porous materials observed by OM and SEM are limited to only the two-dimensional (2D) level, and the realistic three-dimensional (3D) characteristics are not fully reflected in the results [12,13,17,18]. X-ray computed tomography (CT) technology, an advanced technique for 3D quantitative characterization, has been successfully and extensively used in medical, geological, material and other fields. In recent years, many researchers have used micro-CT (which has a micron-level resolution higher than CT) [19] for the 3D quantitative characterization of microporous structures in metallic materials [12,13,17,18,20–22]. Phillion et al. [20] have used a novel semi-solid tensile deformation methodology combined with micro-CT to study the effect of as-cast porosity on the hot tearing behavior of the commercial aluminum magnesium alloy AA5182 and have found that the as-cast porosity was closely linked to the hot tearing susceptibility of aluminum alloys. Seifi et al. [21] have used micro-CT to compare the spatial distribution of internal pores along deposited samples before and after hot isostatic pressing (HIP) of a Ti-48Al-2Cr-2Nb titanium alloy, thus demonstrating that the HIP process can eliminate pore defects. Unfortunately, although micro-CT can be used to analyze the 3D morphology, distribution and quantity of pores in alloys and their influence on the fracture modes of materials, the details of the service process cannot be completely captured, and the effects of the pores on the micromechanical response behavior of materials during the entire damage process cannot be observed in real time.

With the development of computational materials science, computer simulation techniques, an important supplement to experimental investigation, have been extensively used in research on materials. Simulation enables visualization of some details that are difficult to capture in experiments. Consequently, simulation can aid in demonstrating the microscopic properties of materials and their connection with macroscopic mechanical behavior [23,24]. Dunne et al. [16] have proposed a micromechanical model for pore nucleation; studied the nucleation and growth of pores in the titanium alloy IMI834 under high temperature compression deformation; and quantified the stress state sensitivity of pore nucleation. Pushkareva et al. [22] have carried out a crystal plastic finite element (FE) simulation by establishing a 3D approximate geometric model of polycrystalline grains. Through the simulation results, the effect of grain orientation and pore-pore spacing on pore growth in commercial pure titanium was determined. Soro et al. [25] have generated random porous geometries of pure titanium alloys with different porosity by sequentially adding pores with random central coordinates and given shape in a unit cube. The modeling results revealed the evolution of pores during compression deformation and indicated the major roles of pore shape and porosity in determining the mechanical properties. Unfortunately, the relevant simulation calculations were based on ideal mathematical models, algorithms and approximate geometric models, rather than on the realistic microstructures of the materials. The complex and detailed structural information in the materials has not been considered, thus leading to some disagreement between simulations and the experimental results.

In fact, through the CT technique, multiple 2D slice images reflecting the actual structural information of the material can be conveniently obtained, and a 3D model of the microstructure can be rapidly reconstructed with computer software. In this way, some researchers have meshed the generated 3D model and performed numerical simulations of the mechanical behaviors of porous structural materials [17,26,27]. Lu et al. [27] have systematically investigated the as-cast stainless steel 316 L and the titanium alloy Ti-6Al-4 V and studied the 3D micropores for damage prediction in warm-forging through a CT and representative-volume-element approach. Padilla et al. [17] have simulated the evolution of recirculation pores in a single lap joint of a Sn-based solder alloy during shear deformation, and the findings were consistent with the experimental observations. However, the correlation between the fracture path and pore evolution has not yet been discussed in detail, and the underlying mechanism is not well understood.

We performed a finite element simulation of the quasi-static tension based on the realistic microstructure of an as-cast titanium alloy. The material used in the experiments was the $\alpha + \beta$ Ti-5Al-5Nb-1Mo-1V-1Fe alloy, which has pore sizes of 1–2 μm. The micro-CT technique was used to perform 3D microstructure characterization. Subsequently, the damage and fracture in a 3D porous model under a load were simulated and visualized. The modeling results, including mechanical properties and fracture surface morphology, were assessed and quantitatively compared with the observed experimental results. We considered the stress state to analyze the inherent mechanism of crack tip propagation, to better understand the expansion of various pores as well as the dominant factor of fracture path formation at different stages.

2. Materials and experiment

The nominal composition of the Ti-5Al-5Nb-1Mo-1V-1Fe titanium alloy is shown in Table 1. The Al element was added in the form of aluminum scrap, and the Zr element was added in the form of zirconium chips. The Nb, Mo, V and Fe elements were added in the forms of Al—60Nb, Al—60Mo, Al-55 V and Ti—35Fe master alloys. The ingredients were uniformly blended and compacted into cylindrical compacts before the melting process. Then melting stocks were repeatedly smelted three times inside a vacuum induction melting furnace of type VISM-20 (the vacuity was 1.2×10^{-1} Pa, and the operating power was 300 KW). After melting, the melts were poured into an iron mold to form the casting. After cooling to 300 °C, the ingot was removed from the furnace and was air cooled to room temperature.

Three Φ5 mm × 30 mm standard tensile samples with no obvious defects were taken from the as-cast Ti-5Al-5Nb-1Mo-1V-1Fe ingot to carry out the quasi-static tensile tests. Fig. 1(a) and (b) shows the tensile

Table 1
Nominal composition of the Ti-5Al-5Nb-1Mo-1V-1Fe titanium alloy (wt%).

Material	Al	Zr	Nb	Mo	V	Si	Fe	C	O
Ti-5Al-5Nb-1Mo-1V-1Fe	5.0	0.8	5.8	1.5	1.8	0.028	1.0	0.016	0.045

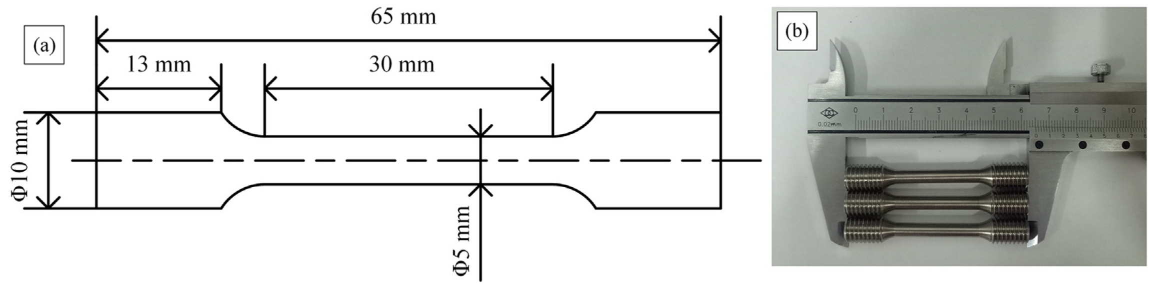

Fig. 1. Tensile sample (a) schematic diagram of the sample specification; (b) the picture of the samples.

sample specification and the picture of the samples, respectively. Φ10 mm × 3 mm samples in the vicinity of tensile samples were taken to perform microstructure observations. The quasi-static tensile tests were carried out at room temperature on an INSTRON 5985 universal testing machine in accordance with the GB/T228.1–2010 tensile test standard. To simulate the quasi-static condition, the displacement rate was fixed at 1.8 mm/min. Afterwards, a type S-4800 scanning electron microscope was used to observe the as-cast microstructure and the microscopic characteristics of the fracture of tensile samples after stretching. Moreover, a Micro VHX-S90B Optical Surface Profiler (Profilometer) was used to characterize the fracture morphology of the tensile samples after stretching.

3. Modeling and finite element simulation methods

3.1. Microstructure-based finite element modeling

Fig. 2 shows the principle of 3D image model reconstruction through micro-CT. The X-ray beam emitted from the X-ray source penetrates a sample (placed on the rotation stage) rotating around z-axis at a constant rotation step φ; the X-ray detector detects and records the ray intensity values through the sample at each rotation angle (the rotation angle will be converted to corresponding spatial coordinate with the translation stage as a reference) to form transmission X-ray images; the intensity values are then converted into digital signals and processed with a back projection algorithm to generate 2D transverse slice images; and then the 2D slices are stacked to reconstruct a 3D image model.

Considering the X-ray penetration capability of micro-CT, a small cylindrical sample of Φ2 mm × 2 mm was used. The sample was scanned with a benchtop Micro-CT (SkyScan 1172) system with 0.7 μm spatial resolution. A uniform high-energy X-ray beam (81 kV and 124 μA) penetrated the sample, and a transmission-coupled device (CCD)-based detector collected the transmitted X-rays. The voxel size of scanning was 0.97 μm × 0.97 μm × 0.97 μm. As illustrated in Fig. 3, 360 transmission X-ray images were acquired while the sample was rotated between 0° and 180° at a rotation step φ of 0.5° and then were cut into 2386 slices along the Z axis in Nrecon (V1.6.9.4, SkyScan 1172) software. Given the low porosity and the small pore size of the sample, the simulation of a large model would entail a large computer operation task. Therefore, the central area with a volume of 80 μm × 80 μm × 80 μm was selected as the region of interest and reconstructed into a 3D image model with the Simpleware commercial package (V7.0, Synopsys). As shown in Fig. 3, the random distribution of the micro-pores could be visualized through hiding the material.

Simpleware also provides a method for automatically transforming the 3D geometrical model into a 3D finite element model (FE model) for numerical simulation. To ensure the stability of calculation, a solid element and hexahedral mesh were used to generate a high quality FE model. As shown in Fig. 4, there were irregularly shaped pores with a size of 1–2 μm internally, as indicated in the red circles. This model was in good agreement with the experimental results detected by SEM, which indicated a pore size of approximately 1.5 μm, as shown

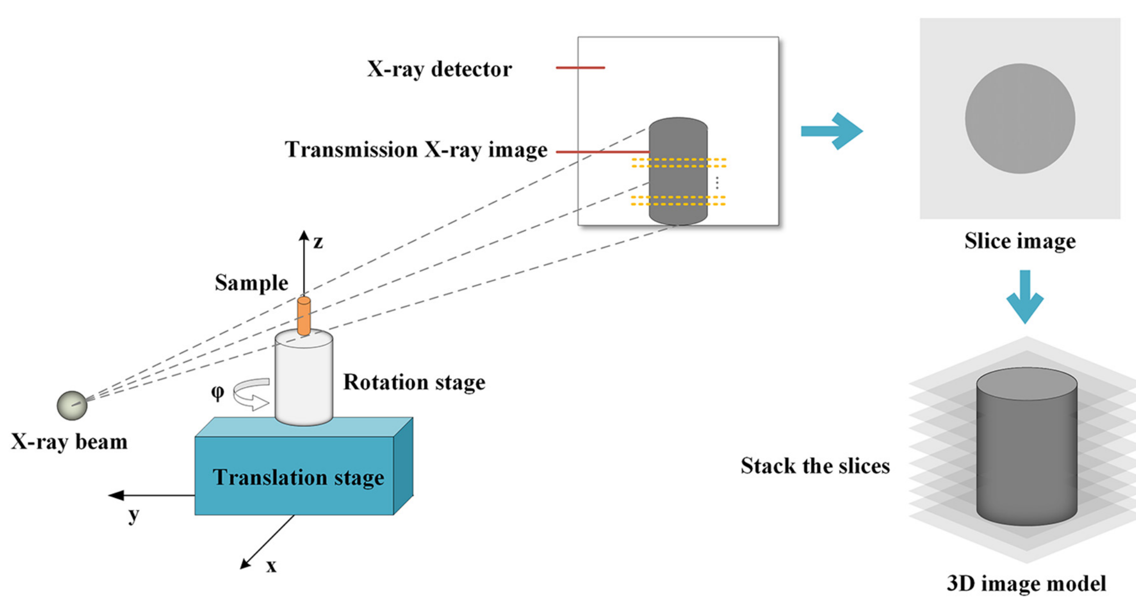

Fig. 2. The principle of 3D image model reconstruction through micro-CT.

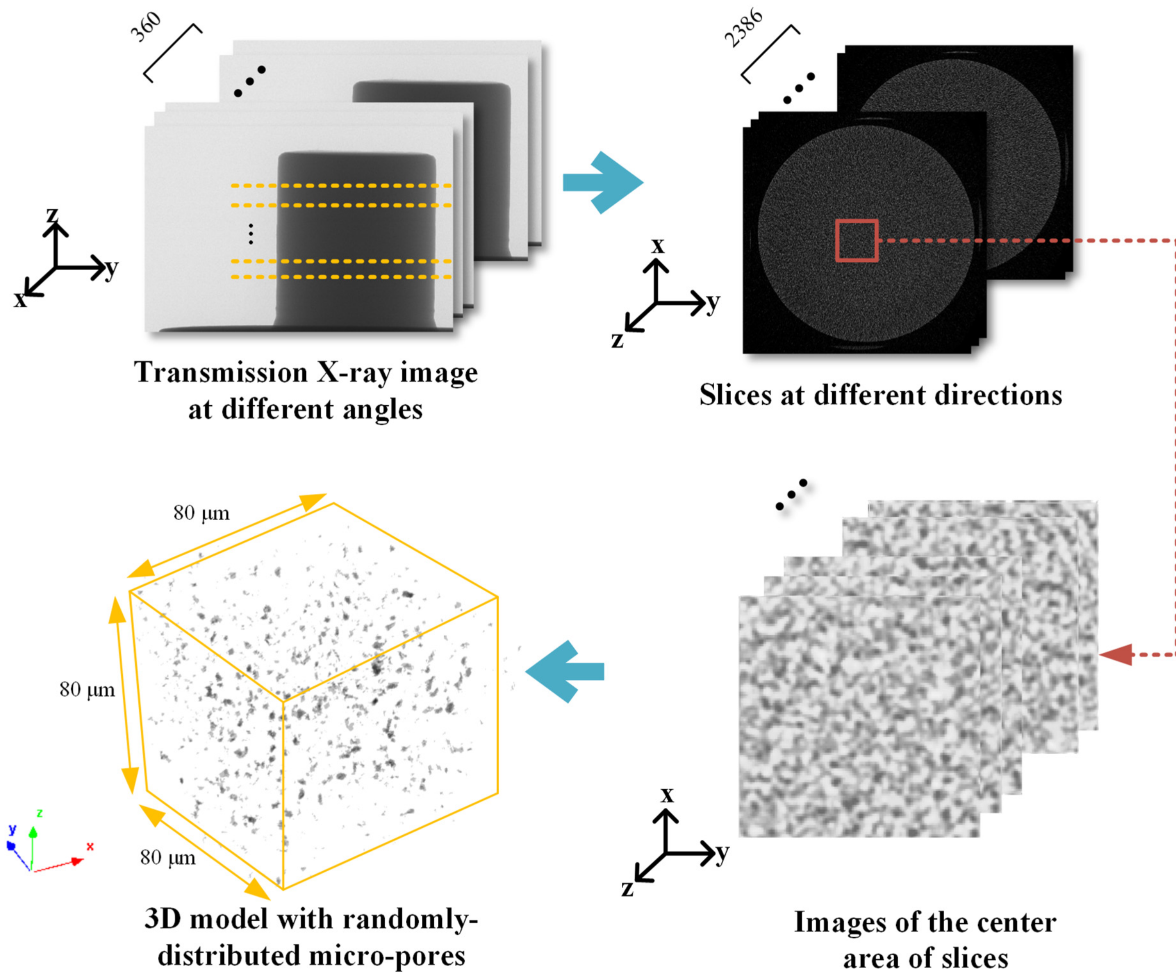

Fig. 3. 3D model reconstruction of the as-cast Ti-5Al-5Nb-1Mo-1V-1Fe alloy.

in the red circles in Fig. 5. Subsequently, the FE model was exported to ANSYS LS-DYNA (V4.2, LSTC) for further calculation.

3.2. Loading definition, boundary conditions and material model

To study the mechanical response of the 3D FE model under the quasi-static tensile load, a changing displacement condition was applied on plane z = 80 μm by prescribing normal displacement with a rate of 9.6×10^{-5} mm/s, as shown in Fig. 6. In addition, the displacements of nodes in the plane z = 0 were fixed.

The material was presumed to be isotropic, and a highly cost effective PLASTIC-KINEMATIC model in LS-DYNA was used. The maximum equivalent plastic strain was defined as the failure criterion, which was determined to be 0.15 through a quasi-static tensile test of hot-

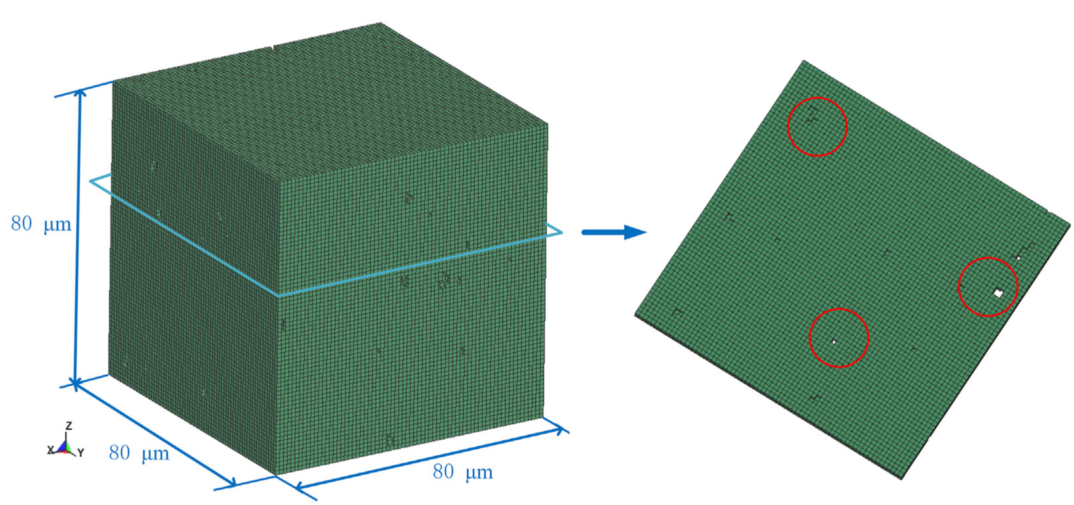

Fig. 4. 3D microstructure-based geometric model and a representative slice.

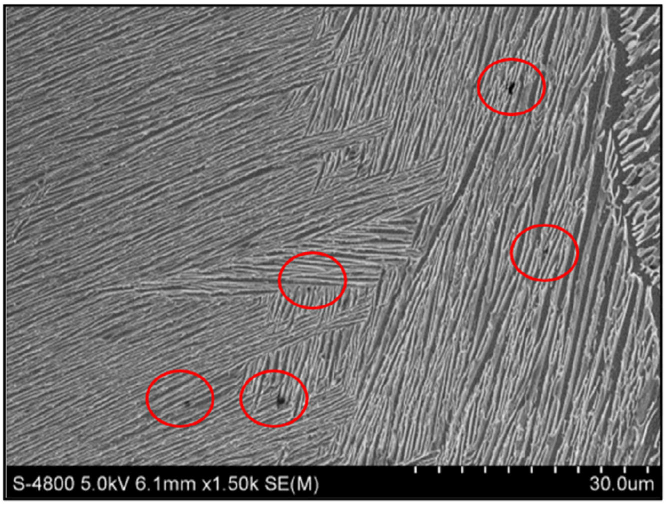

Fig. 5. Microstructure characterization by SEM.

isostatic pressed samples, owing to their nearly non-porous characteristics. During the simulation, when the equivalent plastic strain of a given element satisfied the failure criterion, the element was deleted directly from the model, so the fracture path formation could be tracked. Other primary parameters in the model are listed in Table 2, including the yield stress, tangent modulus, elastic modulus, density and Poisson ratio.

4. Results

4.1. True stress-strain curve

Fig. 7 shows the experimentally measured true stress-true strain curves of three as-cast samples as well as the simulated curve of the overall FE model. In general, the simulated results were in good agreement with the experimental results. The simulated value of fracture strain was 0.066, a value within the experimental range of 0.059–0.069. Moreover, the simulated tensile strength was 1016 MPa, which was also within the experimental value range of 1003–1034 MPa. The simulated yield strength was 920 MPa, a value beyond the experimental range of 860–869 MPa. However, the maximum relative error was only 6.98%, which was quite acceptable. In addition,

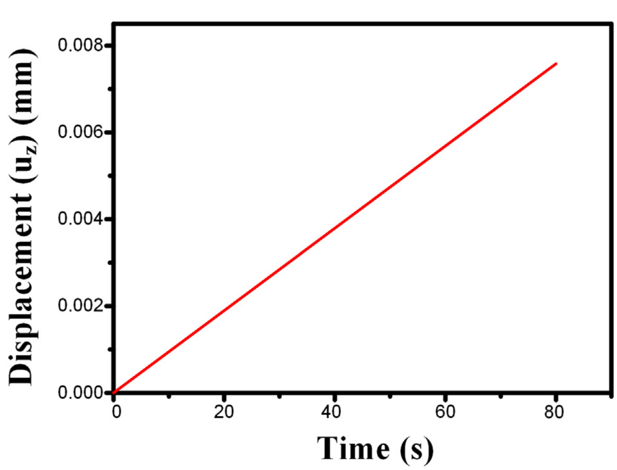

Fig. 6. Displacement-time curve.

Table 2
Primary material parameters properties used in the model.

Yield stress, σ_y (MPa)	Tangent modulus, E_{tan} (MPa)	Elastic modulus, E (GPa)	Density, ρ ($g \cdot cm^{-3}$)	Poisson ratio, ν
930.00	700.23	115.70	4.59	0.322

as shown in Fig. 7, the simulated effective stress nephograms at the macro true-strains of 0.005 and 0.007 represent the stress distribution of the model in the elastic phase; the nephogram at the macro true-strain of 0.009 represents the stress distribution in the yield phase; the nephogram at the macro true-strain of 0.036 represents the stress distribution in the strain-hardening phase; and the nephograms at the macro true-strains of 0.062 and 0.066 represent the stress distribution in the fracture phase. Clearly, the effective stress of the model gradually increased along with the strain until the fracture, at which point the effective stress of the model was released rapidly.

4.2. Fracture morphology

To quantitatively measure the topography of the fracture surface, we characterized the morphology in the micro-region of 110 μm × 80 μm with a Micro XAM-100 Optical Surface Profiler (Profilometer) at a magnification of 3000×, as shown in Fig. 8(a). We found that the height difference between the lowest point and the highest point was 47.09 μm. Fig. 8(b) illustrates the fracture morphology of the FE model, and the predicted topography of the fracture surface is rendered by the z-axis coordinate nephogram. Similar to the experimental observations, the predicted height difference was approximately 50 μm between the lowest point and the highest point. Moreover, the simulated terrain trend was also consistent with the experimental results, which showed an inclination of nearly 45°.

5. Discussion

To quantify the failure process of the 3D FE model, the mass fraction of the failed elements F_{mf} was used as a measure of the degree of failure. The mass fraction of the failed elements F_{mf} is defined by Eq. (1):

$$\mathrm{Fmf} = \frac{m_{failed^{(\varepsilon)}}}{m_{failed^{(\varepsilon_f)}}} \times 100\% \qquad (1)$$

where $m_{failed^{(\varepsilon)}}$ is the mass of the failed elements as a function of the macro true-strain ε, corresponding to the abscissa in Fig. 7, and $m_{failed^{(\varepsilon f)}}$ is the mass of the failed elements at the macro fracture strain ε_f.

Fig. 9 is the mass fraction of the failed elements F_{mf} vs. macro true-strain ε curve of the 3D FE model under the tension load. As shown in the inset of Fig. 9, F_{mf} begun to increase from 0 to a positive value since ε = 0.034, thus illustrating that the failure appeared at ε = 0.034; when 0.034 ≤ ε ≤ 0.049, F_{mf} remained at a rather low value of no >1.0 wt% but showed a gentle upward trend, thus indicating that the crack source gradually formed during this period, which was defined as "Period I" of the failure process and was termed "crack initiation". When 0.049 ≤ ε ≤ 0.06, there was a significant upward trend in F_{mf}, but the rate of change was still relatively slow, thus indicating that the crack underwent steady propagation during this period, which was defined as "Period II" of the failure process and was termed "steady crack propagation". When 0.06 ≤ ε ≤ 0.066, F_{mf} increased immediately from 5.4 wt% to 100 wt%, thus resulting that the crack size reached the critical length at ε = 0.06 and subsequently underwent unstable propagation. The speed of the unstable propagation was extremely high, thus resulting in the rapid failure of the model, and this

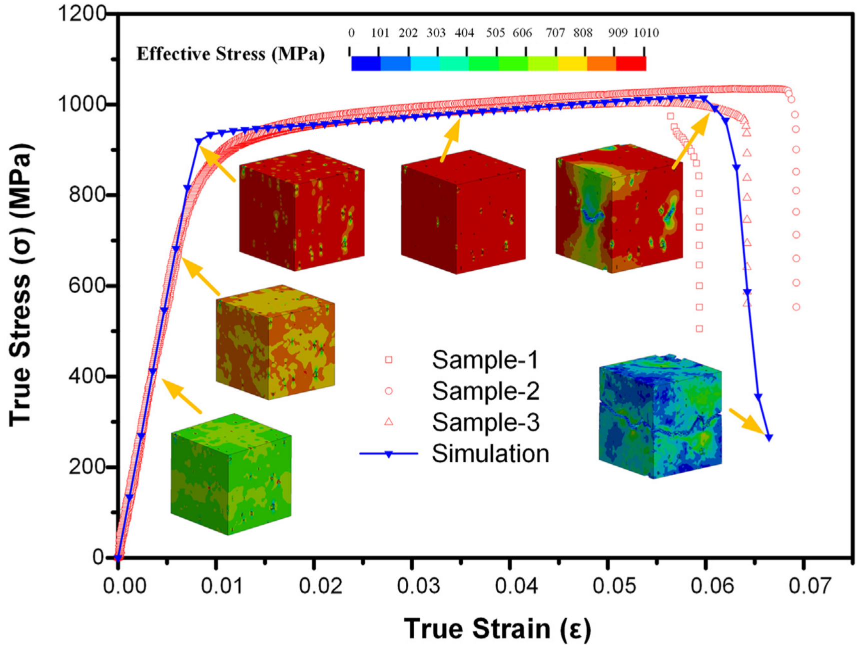

Fig. 7. Experimental and simulated true stress–strain curves.

period was defined as "Period III" of the failure process and was termed "unstable crack propagation".

5.1. Period I-the process of crack initiation

Fig. 10(a) shows the failure contour at $\varepsilon = 0.034$, and the failure elements are explicitly displayed in the model and portrayed in dark green. For a clearer description of the 3D spatial distribution of the crack sources, the non-failure elements are hidden on the basis of Fig. 10(a), as shown in Fig. 10(b). Two cracks were clearly seen to initiate around the micro-pores near the middle region of the side of the model and were labeled crack source 1 and crack source 2, respectively. For investigation of the stress distribution near the initiated crack, the upper half of the model was hidden, because it was ultimately broken into two parts, and the maximum principal stress nephograms at $\varepsilon = 0.034$ and at $\varepsilon = 0.047$, are illustrated in Fig. 10(c) and (d). As shown in Fig. 10(c), there was principal stress concentration around the crack sources and the micro-pores in the model, and the orientation of the maximum principal stress was parallel to the tensile axis; the values of the maximum principal stress in the regions of stress concentration ranged from 1341 MPa to 1955 MPa. As shown in Fig. 10(d), the stress concentration around many micro-pores was more severe, and a new crack, marked crack source 3, was generated. Moreover, crack source 1 and crack source 2 have begun to propagate, and the values of the maximum principal stress changed correspondingly and ranged from 1268 MPa to 1950 MPa.

Clearly, the principal stress concentration, which causes volume deformation and strain concentration, was more likely to appear around the micro-pores than other regions. When the equivalent plastic strain ε_p of some elements around the region of stress concentration met the failure criterion, damage was generated in the way of micro-voids nucleation, thus inducing the initiation of multiple cracks.

5.2. Period II-the process of steady crack propagation

Fig. 11(a) and (b) respectively displays the stress triaxiality nephogram and the effective plastic strain nephogram at $\varepsilon = 0.055$. Fig. 11(a) shows that the stress triaxiality R_σ was the highest near the

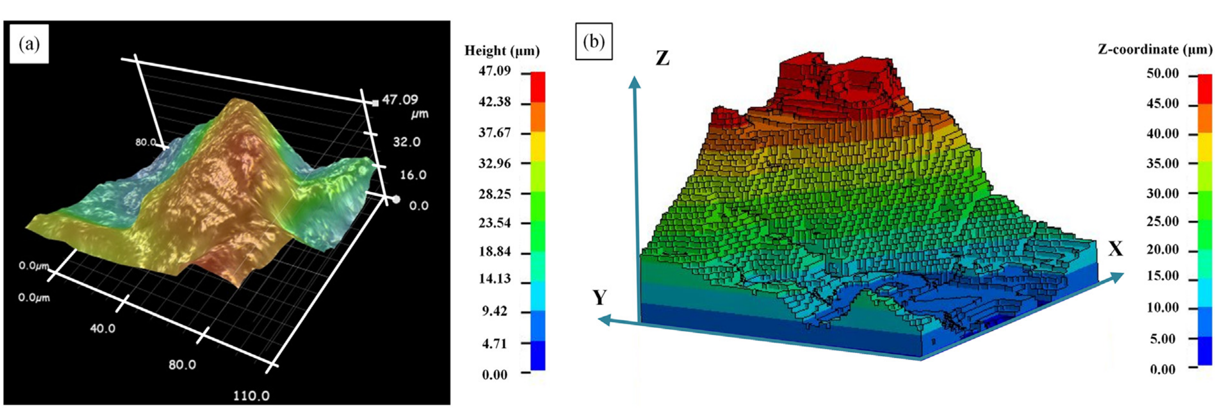

Fig. 8. Fracture morphology (a) experimentally measured results (3000×); (b) simulated results.

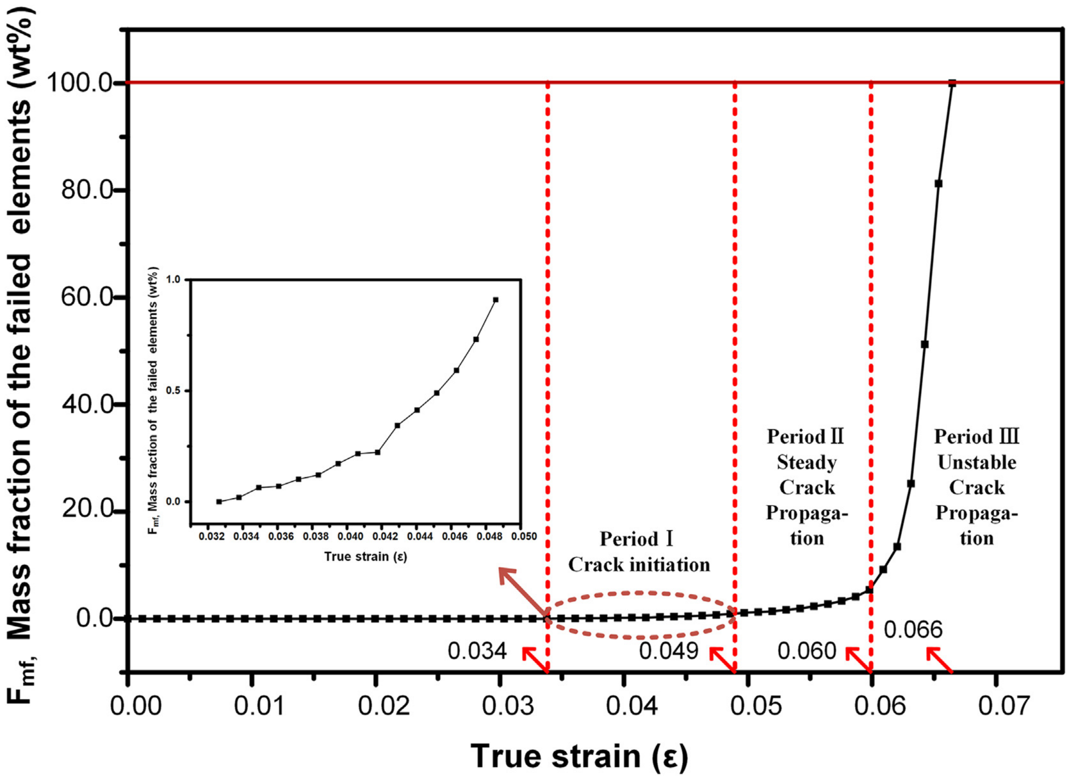

Fig. 9. The mass fraction of the failed elements F_{mf} vs. macro true-strain ε curve.

crack tip, where R_σ was >0.6, thus indicating that the vicinity of the crack tip was in a state of multiaxial tension. Therefore, this region was mainly affected by the hydrostatic stress tensor σ_m and hence had high volumetric energy, which generated new voids and placed constraints on plastic deformation. As shown in Fig. 11(b), the effective plastic strain ε_p in this region was low, ranging from 0.091 to 0.104. However, there was a narrow ring region (marked by a white star) with low R_σ between the crack tip and the ring zone with the highest R_σ (marked by a black star). The R_σ of the narrow ring region ranged from 0.2 to 0.4, thus indicating that this region was under mixed-mode loading of tension-shear and was mainly influenced by the deviatoric stress tensor s_{ij}. Such a stress state placed less of a constraint on plastic deformation, and the strain energy became larger, as can also be confirmed by Fig. 11(b). Fig. 11(b) shows that the effective plastic strain ε_p in this region ranged from 0.104 to 0.130. Such an extremely narrow high deformation further aggravated stress concentration in the vicinity of the crack. Fig. 11(c) shows the maximum principal stress nephogram at $\varepsilon = 0.055$; stress concentration was observed in the ring zone with the highest R_σ around cracks 1 to 5, and the maximum principal stress ranged from 1345 MPa to 2031 MPa, in a direction parallel to the tensile axis.

Fig. 11(d) displays the maximum principal stress nephogram at $\varepsilon = 0.059$. Compared with the maximum principal stress nephogram at $\varepsilon = 0.055$, the stress value in the stress concentration region ranged from 1040 MPa to 2091 MPa, and the peak slightly increased; moreover, cracks 1 to 5 developed on the plane perpendicular to the tensile axis under the tension of the multiaxial principal stress. Fig. 11(e) shows the subsequent maximum principal stress nephogram at $\varepsilon = 0.060$. Compared with the maximum principal stress nephogram at $\varepsilon = 0.059$, cracks 1 to 5 further developed on the plane perpendicular to the tensile axis. Noticeably, crack 1 and crack 4 were nearly connected to each other through void growth and coalescence. These observations indicated that in the period of steady-state propagation, the principal stress was the dominant factor, thereby restricting the size of the zone of plastic deformation, and the corresponding microscopic failure mode was micro-void damage evolution, thus leading to the tensile failure of the model, as a result of the multiaxial tension state. Fig. 11(f) illustrates a typical experimental SEM fracture image, in which nearly equiaxed dimples were seen around the pores (enclosed by the dotted line), and typical ductile failure behavior was observed; these results also verified the failure mode predicted by the simulation results.

5.3. Period III-the process of unstable crack propagation

Fig. 12(a), (b) and (c) shows the stress triaxiality nephogram, the maximum principal stress nephogram and the shear stress nephogram at $\varepsilon = 0.064$, respectively. Three typical regions are marked on these nephograms: ①, ② and ③. The R_σ of region ① ranged from 0.2 to 0.6, which was relatively low and therefore conducive to plastic deformation. As shown in Fig. 12(b) and (c), the maximum principal stress at region ① was relatively low (ranging from 600 MPa to 1152 MPa), but the shear stress was highly concentrated in this region (ranging from 499 MPa to 580 MPa), thus tending to induce shear failure. However, the shear stress of the left side of this region was more severe than that at the right side, possibly because of the short distance and interaction of stress fields between the dense pores on the left side. As for region ② and region ③, which were around crack tips, the stress triaxiality R_σ was >0.6, so the plastic deformation was constrained. As shown in Fig. 12(b) and (c), there existed not only shear stress concentration (ranging from 499 MPa to 580 MPa) but also high principal stress concentration (maximum principal stress concentration ranging from 1428 MPa to 2256 MPa). In addition, Fig. 12(d) shows the effective plastic strain nephogram at $\varepsilon = 0.064$. The left side of region ① showed a local strain concentration that was also the most severe, with ε_p ranging from 0.01 to 0.143; ε_p of the right side of region ① was

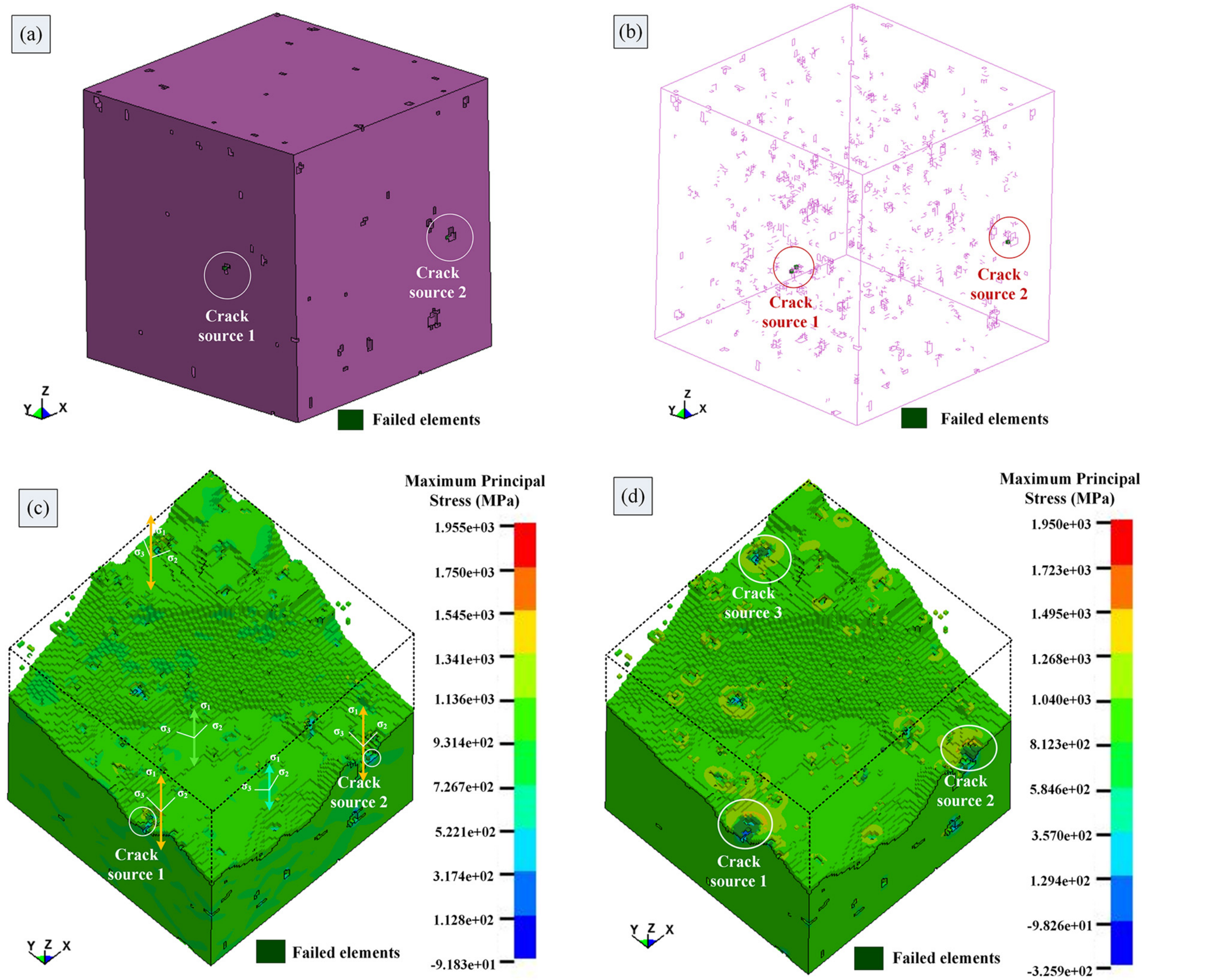

Fig. 10. Simulation results of crack initiation (a) the failure contour of the overall model at ε = 0.034; (b) the failure contour of the model at ε = 0.034 (the non-failure elements are hidden); (c) the maximum principal stress nephogram of the model at ε = 0.034 (the upper half of the model is hidden); (d) the maximum principal stress nephogram of the model at ε = 0.047 (the upper half of the model is hidden).

relatively small, ranging from 0.057 to 0.086; despite the shear concentration within a small range in region ② and region ③, the value of the effective plastic strain was still relatively small, ranging from 0.057 to 0.086, as a result of the constrained effect of principal stress concentration in these two regions on plastic deformation. Therefore, the distribution of effective plastic strain was mainly determined by the combined effects of the shear stress field and the maximum principal stress field.

Fig. 13(a), (b) and (c) displays the stress triaxiality nephogram, the maximum principal stress nephogram and the shear stress nephogram at ε = 0.065, respectively. Compared with the nephograms at ε = 0.064, the elements on the left side of region ① failed under the shear stress concentration, which entailed crack propagation from the plane to the slope at 45° to the tensile axis, namely extension to a plane parallel to the max shear stress. Meanwhile, the elements of regions ② and ③ failed under the mixed effects of the principal stress concentration and shear stress concentration, thus causing the crack to propagate on the plane (vertical to tensile axis) to a small extent. In addition, Fig. 13(a) shows that the R_σ of the region (surrounded by a quadrilateral frame) was relatively low, ranging from 0 to 0.4, thus indicating that this region was inclined to shear failure. As shown in Fig. 13(b) and (c), the maximum principal stress was low, ranging from −393 MPa to 1418 MPa, whereas the shear stress concentration was severe, up to 578 MPa. Furthermore, Fig. 13(d) shows the maximum principal nephogram at ε = 0.066. The crack ran through a 45° slope under shear stress concentration compared with the nephograms at ε = 0.065. The abrupt failure of the model led to a sharp decrease in the maximum principal stress value, with a maximum decline value of 1044 MPa. Therefore, in the period of unstable crack propagation, the shear stress gradually became the dominant factor, and the corresponding microscopic failure mode gradually changed from micro-void damage evolution to cleavage and plastic slip, thus resulting in rapid shear failure. Fig. 13(e) and (f) respectively illustrate the micro shear plane near the crack (enclosed by the dotted line) and the river pattern of the sample fracture characterized by SEM, indicating mixed failure behavior and confirming the failure mode predicted by the simulation results.

6. Conclusions

A 3D microscopic model reflecting the realistic microstructural characteristics of as-cast Ti-5Al-5Nb-1Mo-1V-1Fe was established by using micro-CT and FE techniques. Subsequently, the model was used to

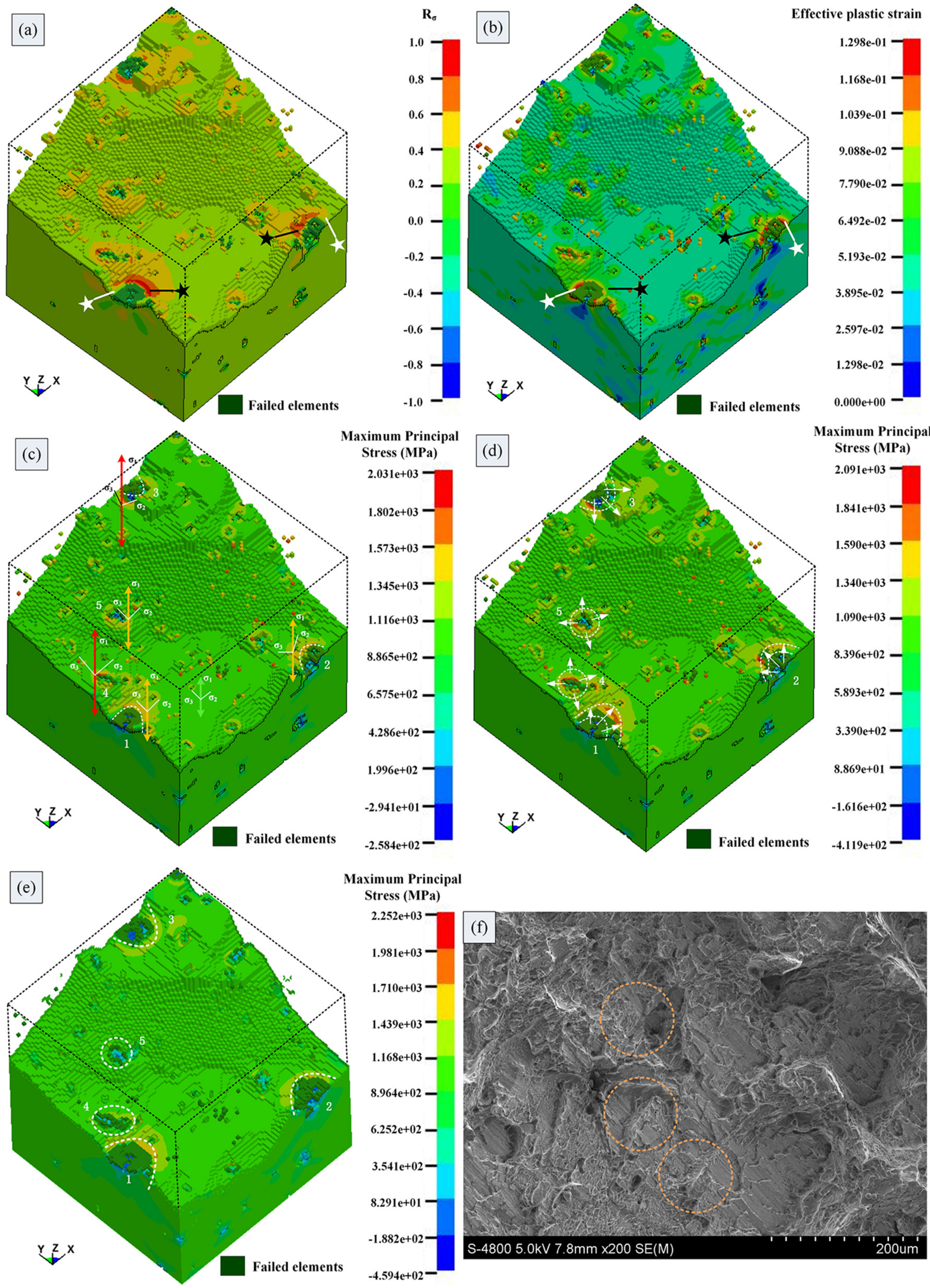

Fig. 11. Simulation and experimental results of steady crack propagation (a) the stress triaxiality nephogram at ε = 0.055; (b) the effective plastic strain nephogram at ε = 0.055; (c) the maximum principal stress nephogram at ε = 0.055; (d) the maximum principal stress nephogram at ε = 0.059; (e) the maximum principal stress nephogram at ε = 0.060; (f) nearly equiaxed dimples on a small plane perpendicular to the axis of tension by SEM.

study the 3D evolution process of the damage and failure mechanism under quasi-static uniaxial tension by using FE techniques, and the simulation results were consistent with the experimental observations. The principal findings are summarized as follows:

(1) At the initiation of loading, principal stress concentration existed around two micro-pores near the middle region of the side of the model; the effective plastic strain in this region first satisfied failure criterion, so that two initial crack sources were generated. As

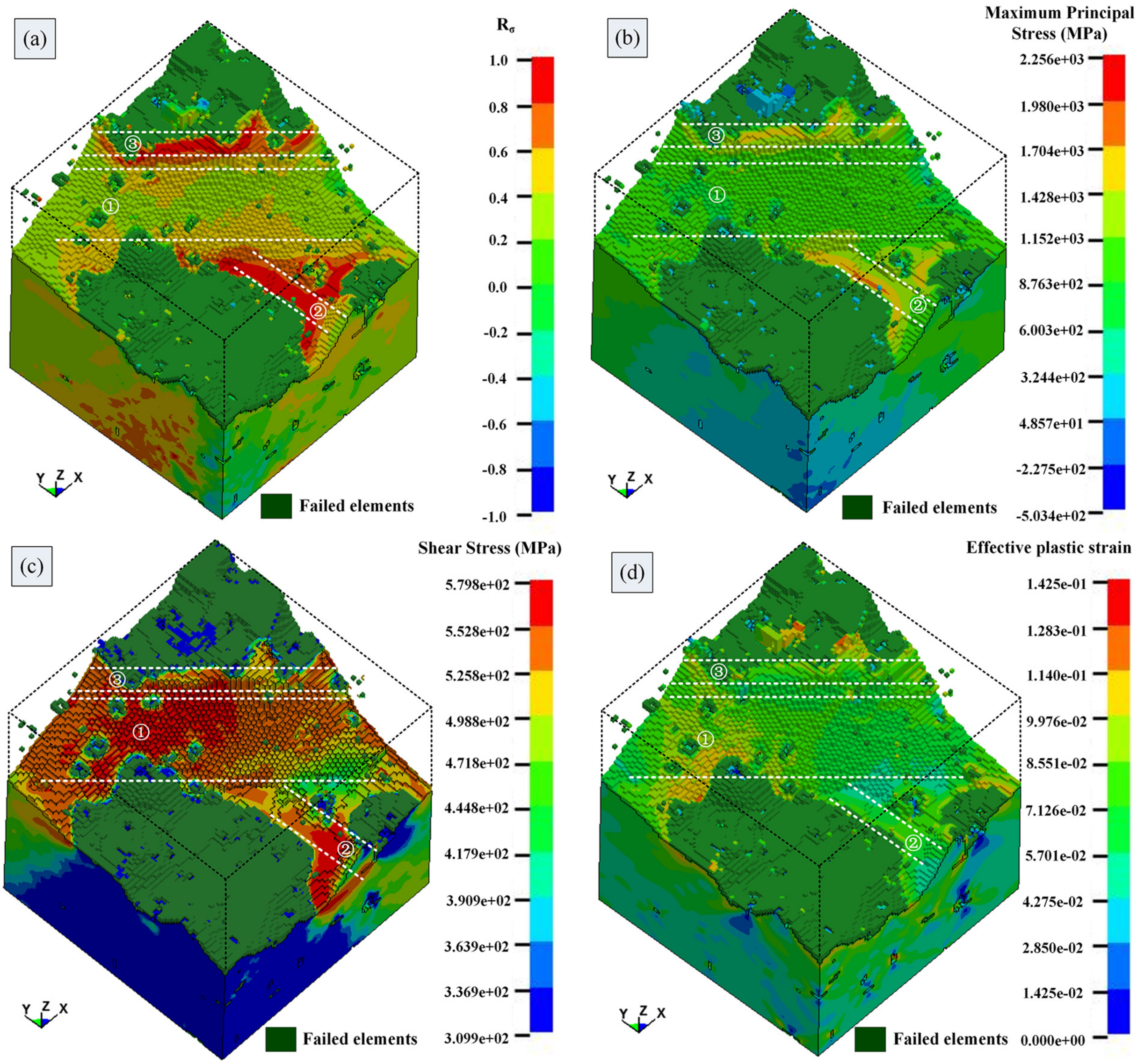

Fig. 12. Simulation results of the model at $\varepsilon = 0.064$ (a) the stress triaxiality nephogram; (b) the maximum principal stress nephogram; (c) the shear stress nephogram; (d) the effective plastic strain nephogram.

loading continued, the stress concentration around the micro-pores became more severe, and new crack sources were constantly generated inside the model.

(2) In the period of steady crack propagation, the stress triaxiality R_σ of the region near the crack tip was >0.6, and multiaxial principal stress concentration existed in this region; therefore, the microscopic failure mode was micro-void damage evolution and was inclined to induce tensile failure. In addition, there was a narrow ring region with low R_σ (0.2–0.4) between the crack tip and the ring zone with the highest R_σ. Severe plastic deformation was generated in this narrow region, thereby further aggravating the stress concentration near the cracks.

(3) In the period of unstable crack propagation, the R_σ of the region between the cracks, which reached the critical size, was relatively low (0–0.6), and shear stress concentration existed in this region; shear stress concentration gradually became the dominant factor affecting failure, thus inducing severe plastic deformation concentration. Consequently, the microscopic failure mode gradually became plastic slip and cleavage, thereby resulting in the final, rapid shear failure of the model.

CRediT authorship contribution statement

Haichao Gong: Investigation, Writing-original draft. **Qunbo Fan:** Conceptualization, Methodology, Supervision. **Yu Zhou:** Formal analysis. **Duoduo Wang:** Formal analysis. **Pengru Li:** Formal analysis. **Tiejian Su:** Resources. **Hongmei Zhang:** Project administration.

Acknowledgments

This work was supported by the National Natural Science Foundation of China (Grant No. 51571031).

Data availability statement

The raw/processed data required to reproduce these findings cannot be shared at this time as the data also forms part of an ongoing study.

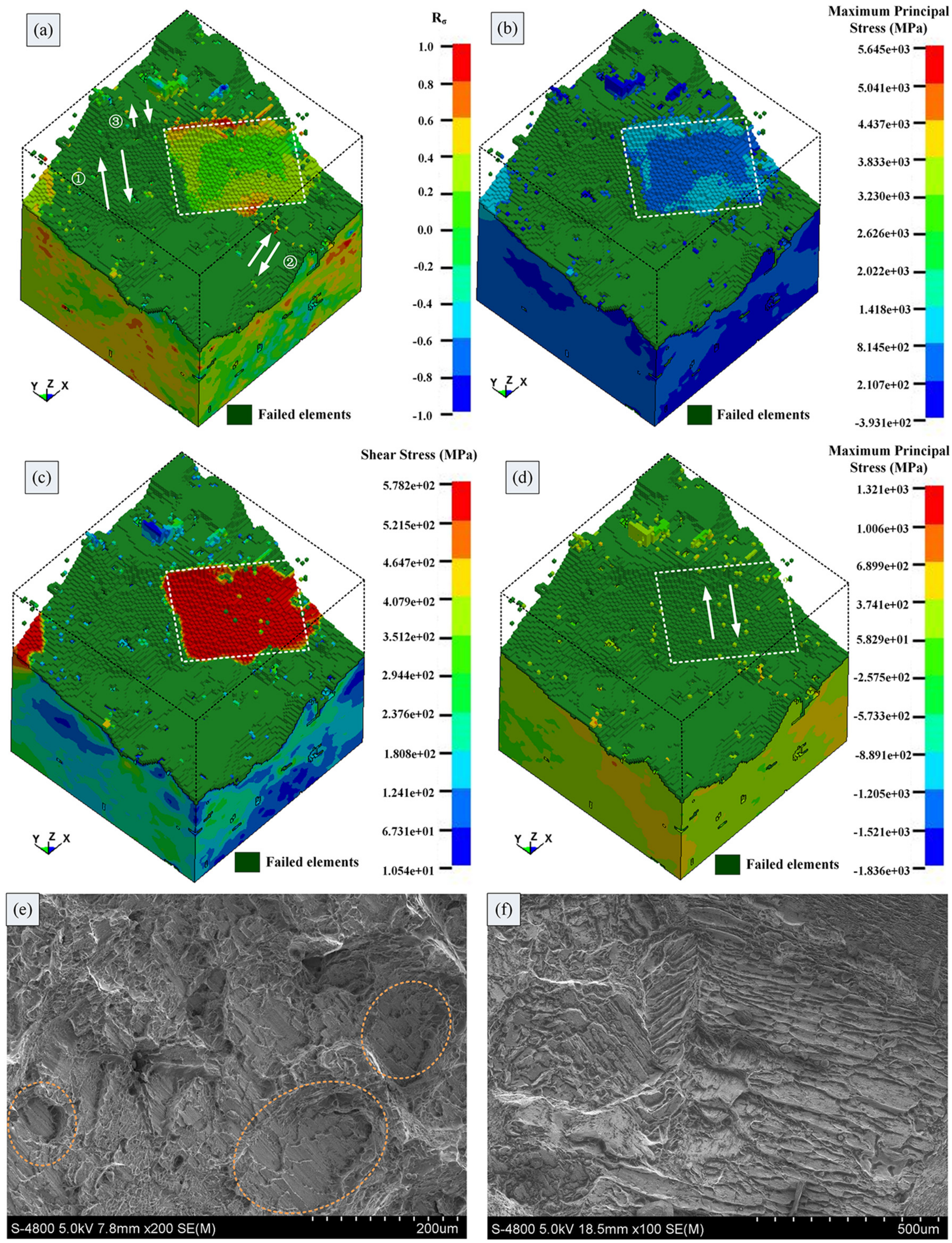

Fig. 13. Simulation and experimental results of unstable crack propagation (a) the stress triaxiality nephogram at $\varepsilon = 0.065$; (b) the maximum principal stress nephogram at $\varepsilon = 0.065$; (c) the shear stress nephogram at $\varepsilon = 0.065$; (d) the maximum principal stress nephogram at $\varepsilon = 0.066$, (e) micro shear plane near crack observed by SEM; (f) river pattern observed by SEM.

References

[1] A.S. Khan, Y.S. Suh, R. Kazmi, Quasi-static and dynamic loading responses and constitutive modeling of titanium alloys, Int. J. Plast. 20 (2004) 2233–2248, https://doi.org/10.1016/j.ijplas.2003.06.005.

[2] D. Banerjee, J.C. Williams, Perspectives on titanium science and technology, Acta Mater. 61 (2013) 844–879, https://doi.org/10.1016/j.actamat.2012.10.043.

[3] S.D. Meshram, T. Mohandas, A comparative evaluation of friction and electron beam welds of near-α titanium alloy, Mater. Des. 31 (2010) 2245–2252, https://doi.org/10.1016/j.matdes.2009.10.012.

[4] C.Y. Li, H.Y. Wang, S.P. Wu, et al., Research on mould filling and solidification of titanium alloy in vertical centrifugal casting, Rare Metal Mat. Eng. 39 (2010) 388–392, https://doi.org/10.1016/S1875-5372(10)60085-9.

[5] A. Agarwal, E. Basile, J. Bowler, et al., Alternative technologies and design for metallic parts in aviation: The use of titanium investment casting for aircraft structural components, Aircraft Structural Design Conference, London, 2016.

[6] H. Attar, S. Ehtemam-Haghighi, D. Kent, et al., Comparative study of commercially pure titanium produced by laser engineered net shaping, selective laser melting and casting processes, Mater. Sci. Eng. A 705 (2017) 385–393, https://doi.org/10.1016/j.msea.2017.08.103.

[7] V.B. Vykhodets, T.E. Kurennykh, N.Y. Tarenkova, Identification of the sources of gas-containing metallurgical defects during the smelting of titanium alloys, Russ. J. Nondestruct. 47 (2011) 176–188, https://doi.org/10.1134/S1061830911030119.
[8] S.Y. Zhang, J.S. Li, H.C. Kou, et al., Numerical modeling and experiment of counter-gravity casting for titanium alloys, Int. J. Adv. Manuf. Tech. 85 (2016) 1877–1885, https://doi.org/10.1007/s00170-015-8167-y.
[9] N.Y. Tarenkova, V.B. Vykhodets, V.A. Krashaninin, et al., Formation of gas-saturated defects in titanium alloys during vacuum-arc remelting, Russ. Metall. (2) (2011) 127–132, https://doi.org/10.1134/S0036029511020145.
[10] Y.J. Yan, G.R.L. Nash, P. Nash, Effect of density and pore morphology on fatigue properties of sintered Ti–6Al–4V, Int. J. Fatigue 55 (2013) 81–91, https://doi.org/10.1016/j.ijfatigue.2013.05.015.
[11] A.R. Ragab, C.A.R. Saleh, Evaluation of constitutive models for voided solids, Int. J. Plast. 15 (1999) 1041–1065, https://doi.org/10.1016/S0749-6419(99)00024-8.
[12] O. Lashkari, L. Yao, S. Cockcroft, et al., X-ray microtomographic characterization of porosity in aluminum alloy A356, Metall. Mater. Trans. A 40 (2009) 991–999, https://doi.org/10.1007/S11661-008-9778-9.
[13] H. Shen, S.M. Oppenheimer, D.C. Dunand, et al., Numerical modeling of pore size and distribution in foamed titanium, Mech. Mater. 38 (2006) 933–944, https://doi.org/10.1016/j.mechmat.2005.06.027.
[14] Q. Ye, G. He, In-situ formed graded microporous structure in titanium alloys and its effect on the mechanical properties, Mater. Des. 83 (2015) 295–300, https://doi.org/10.1016/j.matdes.2015.06.066.
[15] W. Chen, C. Chen, X.H. Zi, et al., Controlling the microstructure and mechanical properties of a metastable β titanium alloy by selective laser melting, Mater. Sci. Eng. A 726 (2018) 240–250, https://doi.org/10.1016/j.msea.2018.04.087.
[16] F.P.E. Dunne, I. Katramados, Micro-mechanical modelling of strain induced porosity under generally compressive stress states, Int. J. Fatigue 14 (1998) 577–595, https://doi.org/10.1016/S0749-6419(99)80001-1.
[17] E. Padilla, V. Jakkali, L. Jiang, et al., Quantifying the effect of porosity on the evolution of deformation and damage in Sn-based solder joints by X-ray microtomography and microstructure-based finite element modeling, Acta Mater. 60 (2012) 4017–4026, https://doi.org/10.1016/j.actamat.2012.03.048.
[18] O. Kuwazuru, Y. Murata, Y. Hangai, et al., X-ray CT inspection for porosities and its effect on fatigue of die cast aluminium alloy, J. Solid Mech. Mater. Eng. 2 (2008) 1220–1231, https://doi.org/10.1299/jmmp.2.1220.
[19] S.R. Stock, Recent advances in X-ray microtomography applied to materials, Int. Mater. Rev. 53 (2008) 129–181, https://doi.org/10.1179/174328008X277803.
[20] A.B. Phillion, S.L. Cockcroft, P.D. Lee, A new methodology for measurement of semi-solid constitutive behavior and its application to examination of as-cast porosity and hot tearing in aluminum alloys, Mater. Sci. Eng. A 491 (2008) 237–247, https://doi.org/10.1016/j.msea.2008.01.078.
[21] M. Seifi, A.A. Salem, D.P. Satko, et al., Effects of HIP on microstructural heterogeneity, defect distribution and mechanical properties of additively manufactured EBM Ti-48Al-2Cr-2Nb, J. Alloy. Compd. 729 (2017) 1118–1135, https://doi.org/10.1016/j.jallcom.2017.09.163.
[22] M. Pushkareva, J. Adrien, E. Maire, et al., Three-dimensional investigation of grain orientation effects on void growth in commercially pure titanium, Mater. Sci. Eng. A 671 (2016) 221–232, https://doi.org/10.1016/j.msea.2016.06.053.
[23] I. Balasundar, T. Raghu, Experimental and numerical investigation on the tensile properties of a titanium alloy disc with dual microstructure, Mater. Sci. Eng. A 706 (2017) 104–114, https://doi.org/10.1016/j.msea.2017.08.097.
[24] R. Guerchais, F. Morel, N. Saintier, Effect of defect size and shape on the high-cycle fatigue behavior, Int. J. Fatigue 100 (2017) 530–539, https://doi.org/10.1016/j.ijfatigue.2016.12.010.
[25] N. Soro, L. Brassartb, Y.H. Chen, et al., Finite element analysis of porous commercially pure titanium for biomedical implant application, Mater. Sci. Eng. A 725 (2018) 43–50, https://doi.org/10.1016/j.msea.2018.04.009.
[26] H.Y. Wang, W.J. Hu, F.P. Zhao, Numerical simulation of quasi-static compression on a complex rubber foam, Acta Mech. Solida Sin. 30 (2017) 285–290, https://doi.org/10.1016/j.camss.2017.03.009.
[27] X.Z. Lu, L.C. Chan, Micro-voids quantification for damage prediction in warm forging of biocompatible alloys using 3D X-ray CT and RVE approach, J. Mater. Process Tech. 258 (2018) 116–127, https://doi.org/10.1016/j.jmatprotec.2018.03.020.